Materials Science & Engineering C 130 (2021) 112456

Contents lists available at ScienceDirect

Materials Science & Engineering C

journal homepage: www.elsevier.com/locate/msec

mSLA-based 3D printing of acrylated epoxidized soybean oil - nano-hydroxyapatite composites for bone repair

Dibakar Mondal [a], Zahra Haghpanah [a,c], Connor J. Huxman [a], Sophie Tanter [a,b], Duo Sun [c], Maud Gorbet [c], Thomas L. Willett [a,*]

[a] Composite Biomaterial Systems Laboratory, University of Waterloo, Canada
[b] Université de Technologie de Compiègne, France
[c] Material Interaction with Biological Systems Laboratory, University of Waterloo, Canada

ARTICLE INFO

Keywords:
Nanocomposite
3D printing
Masked stereolithography
Bone repair
Acrylated epoxidized soybean oil
Nanohydroxyapatite

ABSTRACT

Structural bone allografts are used to treat critically sized segmental bone defects (CSBDs) as such defects are too large to heal naturally. Development of biomaterials with competent mechanical properties that can also facilitate new bone formation is a major challenge for CSBD repair. 3D printed synthetic bone grafts are a possible alternative to structural allografts if engineered to provide appropriate structure with sufficient mechanical properties. In this work, we fabricated a set of novel nanocomposite biomaterials consisting of acrylated epoxidized soybean oil (AESO), polyethylene glycol diacrylate (PEGDA) and nanohydroxyapatite (nHA) by using masked stereolithography (mSLA)-based 3D printing.

The nanocomposite inks possess suitable rheological properties and good printability to print complex, anatomically-precise, 'by design' grafts. The addition of nHA to the AESO/PEGDA resin improved the tensile strength and fracture toughness of the mSLA printed nanocomposites, presumably due to small-scale reinforcement. By adding 10 vol% nHA, tensile strength, modulus and fracture toughness (K_{Ic}) were increased to 30.8 ± 1.2 MPa (58% increase), 1984.4 ± 126.7 MPa (144% increase) and 0.6 ± 0.1 MPa·m$^{1/2}$ (42% increase), respectively (relative to the pure resin). The nanocomposites did not demonstrate significant hydrolytic, enzymatic or oxidative degradation when incubated for 28 days, assuring chemical and mechanical stability at early stages of implantation. Apatite nucleated and covered the nanocomposite surfaces within 7 days of incubation in simulated body fluid. Good viability and proliferation of differentiated MC3T3-E1 osteoblasts were also observed on the nanocomposites. Taken all together, our nanocomposites demonstrate excellent bone-bioactivity and potential for bone defect repair.

1. Introduction

Precision technologies for fabrication of three-dimensional (3D) nanocomposite bone grafts are emerging rapidly with advancement in additive manufacturing techniques and synthesis of bone-bioactive polymeric biomaterials [1–5]. Compared to traditional fabrication methods including casting, injection molding, *etc.*, 3D printing provides advantageous freedom in design and fabrication of complex, hierarchical and patient-specific geometries [6]. Materials with appropriate functionality, mechanical properties, degradation behavior and bioactivity can be processed into complex shapes with the help of computer-aided design (CAD) and an appropriate 3D printer [7–10].

Masked stereolithography (mSLA), a distinct format of vat photopolymerization 3D printing, is a high-resolution light-assisted printing process where a light/UV sensitive liquid resin is solidified (cured) *via* light/UV exposure in a layer-by-layer process. Compared to other 3D printing techniques, such as fused deposition modeling (FDM) or stereolithography (SLA), mSLA printing methods are cost effective, defect-free and relatively fast, due to the printing of each layer all at once rather than point-by-point [2].

Over the last decade, selection and development of materials as inks for mSLA-based 3D printing have progressed significantly [6]. Among the vast library of photocurable polymers, the choice of polymers for bone repair and replacement is limited due to the desire for controlled degradation *via* cell-mediated remodeling, superior mechanical strength and excellent bioactivity. Natural polymers can be better choices than

* Corresponding author.
E-mail address: thomas.willett@uwaterloo.ca (T.L. Willett).

https://doi.org/10.1016/j.msec.2021.112456
Received 29 June 2021; Received in revised form 8 September 2021; Accepted 22 September 2021
Available online 29 September 2021

synthetic polymers as they generally have good biocompatibility and non-cytotoxic biodegradation products.

AESO is a plant-derived triglyceride, functionalized with acrylate groups and is an excellent candidate for photopolymerization-based 3D printing for biomedical applications [11–13]. AESO-based polymeric composites afford eco-friendly and renewable ways to fabricate biomaterials. The triglycerides in AESO consist of natural fatty acids with negligible cytotoxicity. Nano-scale hydroxyapatite (nHA) particles are similar to natural bone mineral in their chemical nature. They demonstrate bioactivity and osteoconductivity when studied *in vitro* and *in vivo* [14–16].

In our previous studies, we have 3D printed AESO/nHA/PEGDA nanocomposites using Direct Ink Writing (DIW) [19–21]. These nanocomposites had excellent mechanical properties and cell-material interactions. While DIW is a tedious process, it is very convenient for printing porous 3D scaffolds using AESO/nHA/PEGDA nanocomposite inks with high nHA volume fraction. However, 3D printing of flawless, non-porous complex nanocomposite grafts using DIW is a major challenge due to the rheological properties of the inks.

In mSLA-based 3D printing, it is crucial to have an ink viscosity low enough so that the build platform can move freely through the ink and the ink can refill the small gap between the printed object and bottom of the ink tray. The recommended viscosity for ceramic-based nanocomposite inks is ~5 Pa·s or lower [2,6,17,18]. AESO is a viscous monomer with a molecular mass of approximately 1200 Da and a viscosity of 25 Pa·s at room temperature [13]. To efficiently print an AESO/nHA-based nanocomposite ink using mSLA, a thinning reagent is required to reduce the overall ink viscosity and improve the mechanical properties of the 3D printed nanocomposites. PEGDA has two acrylate groups and very low viscosity (~0.025 Pa·s) that help to reduce the overall viscosity of AESO/nHA ink and improves the mechanical properties by increasing the crosslinking density.

In this work, we studied the effect of nanohydroxyapatite content (5 and 10 vol%) on viscosity and printability of AESO/nHA/PEGDA nanocomposites for mSLA-based 3D printing. To the best of our knowledge, there are no studies in the available literature on mSLA-based 3D printing of AESO-nHA-nanocomposites for bone reconstruction or tissue engineering applications. We hypothesized that the addition of nHA to the AESO/PEGDA resin would improve the strength, fracture toughness, cytocompatibility, and bioactivity of the mSLA-printed nanocomposites. We evaluated the tensile and fracture mechanical properties of 3D printed nanocomposite specimens. We measured water absorption, hydrolytic, enzymatic and oxidative biodegradation *in vitro* of these 3D printed nanocomposites. Bone-bioactivity and cytocompatibility of the nanocomposites were evaluated by apatite deposition in simulated body fluid (SBF) and by studying the adhesion and proliferation of differentiated MC3T3-E1 osteoblasts on the nanocomposite surfaces, respectively.

2. Materials and methods

2.1. Materials

AESO, PEGDA (MW 250) and Phenylbis(2,4,6-trimethylbenzoyl) phosphine oxide (Irgacure 819) were purchased from Sigma-Aldrich Co. H^1-NMR shows 3–4 acrylate groups per AESO molecule and the absence of residual epoxide functional groups [21]. Nanohydroxyapatite powder (nHA, calcium-deficient, rod-shaped, aspect ratio 3–4 with approximately 120 nm length) was purchased from MKNano (M K Impex Corp., Mississauga, Canada) [22]. This nHA has a calcium-to-phosphorous ratio of ~1.52, with specific gravity of 2.92 and an approximate crystallinity index of 0.52–0.54 [22]. All chemicals were used as received.

2.2. Preparation of nanocomposite inks

AESO and PEGDA were blended using an ultrasonic homogenizer (Branson Sonifier 450, Emerson Inc., USA) for 5 min. Then, Irgacure 819 photoinitiator was dissolved in this resin mixture at 1% of total ink volume using an ultrasonic homogenizer. nHA powder was then added to the mixture and dispersed using the ultrasonic homogenizer for 30 min. The ratio of AESO: PEGDA was kept constant for all inks at 1:1. This ratio was chosen based on the classic rule of mixtures in order to maintain the viscosity of the AESO/PEGDA ink in the optimum range for mSLA-based 3D printing. Four inks were prepared and their compositions are summarized in Table 1.

2.3. Characterization of the nanocomposite inks

2.3.1. Cure depth measurements

The required UV exposure time and intensity to fully cure each print layer were determined first by conducting standard cure-depth experiments using an adapted protocol [23]. The nanocomposite inks were loaded in cylindrical opaque PTFE molds and exposed to known doses of UV light (BlueWave® QX4® LED Spot-Curing System, Dymax Corp., USA) at one end of the cylindrical hole. The thickness of the cured material was measured by using calipers after rinsing away the uncured residue with ethanol ($n = 6$). The standard cure-depth equation [24],

$$C_d = D_p ln\left(\frac{E_{max}}{E_c}\right)$$

where C_d is the cure depth, E_{max} is the energy dosage per area, E_c represents the critical energy dosage, and D_p is the depth of penetration, was fit to the experimental data. E_{max} is constant for an mSLA printer with constant settings so the C_d or, in this context, maximum layer height of each nanocomposite ink, was calculated from the corresponding standard cure-depth curve. To achieve successful curing during mSLA-based 3D printing, the layer height was set to less than the calculated cure depth value.

2.3.2. Rheology of the nanocomposite inks

The rheological properties of the nanocomposite inks were measured using a Bohlin CS Rheometer with a cone and plate geometry (CP 4/40, with 150 μm gap). The inks for this experiment were prepared without photo-initiator and all measurements were performed at room temperature under shear strain rates from 0.01 s^{-1} and 100 s^{-1} ($n = 3$). At each shear strain rate, the viscosity and shear stress were recorded at 10 s intervals.

2.4. mSLA-based 3D printing of nanocomposite inks

mSLA-based 3D printing was conducted using an Anycubic Photon (Anycubic Inc., China). 3D stereolithographic files were sliced using the Anycubic Photon slicer software. All specimens were printed by setting the layer height to 50 μm. This layer height value is less than the lowest calculated cure depth value among the nanocomposite inks. Each layer was exposed to UV for 50 s except for the first six layers which were cured for 60 s to ensure good build plate adhesion. After completion of 3D printing, the specimens were removed from the print bed using a metal spatula and wiped thoroughly. To avoid uncured ink residue on the surface, specimens were exposed to additional UV in a post-print

Table 1
Compositions of AESO/PEGDA/nHA nanocomposite inks.

Inks	AESO (vol%)	PEGDA (vol%)	nHA (vol%)
SP0	50	50	0
SP5	47.5	47.5	5
SP10	45	45	10
SP15	42.5	42.5	15

curing chamber for an hour on each side, and then rinsed with ethanol.

2.5. Characterization of 3D printed nanocomposite

The efficiency of curing and conversion was measured by Fourier Transform Infra-Red spectroscopy (FTIR) analysis of 3D printed cylindrical discs (10 mm in diameter and 1 mm in thickness; $n = 3$). FTIR spectra were obtained using a Nicolet 6700 FT-IR Spectrometer (Thermo Scientific, USA) at a resolution of 4 cm^{-1} with a sample scan of 32. All spectra were analyzed using OMNIC series software.

The organic-inorganic ratios and thermal decomposition behavior of the 3D printed nanocomposites were measured using thermogravimetric analysis (TGA). Approximately 10 mg of each 3D printed nanocomposite specimen ($n = 3$) were heated and burnt in a TA Q500 (TA Instruments Inc., New Castle, DE) from 25 to 800 °C under air atmosphere at 10 °C/min heating rate. The remaining mass after burnout was considered as the inorganic content and used to calculate the organic-inorganic ratio of each nanocomposite specimen. Differential scanning calorimetry (DSC) was conducted to measure the glass transition temperature (T_g). All experiments were carried out under nitrogen flow (50 mL/min) using a TA Q2000 (TA instruments Inc., New Castle, DE). 3D printed nanocomposite specimens (~8 mg, n = 3) were sealed in aluminum pans and heated from −40 °C to 400 °C at 5 °C/min.

Printability of the nanocomposite inks was evaluated by image analysis of mSLA printed lattice cubes. The area of each pore was measured and compared with theoretical values. 3D printed blocks were imaged using a digital camera (Canon EOS REBEL T7i) mounted on a macroscope (LM Macroscope 9×, Micro Tech Lab, Austria). The pore area was calculated using ImageJ (ImageJ 1.52a, NIH). The theoretical (designed) value of the pore area was 1 mm^2. The printability was calculated as:

$$Printability, Pr = \frac{Single\ pore\ area\ in\ 3D\ printed\ block}{Single\ pore\ area\ in\ designed\ block}$$

If the object printed perfectly, the area of the pores would be same as designed and Pr would be equal to 1.

2.6. Printing and tensile testing of the nanocomposites

Dogbone-shaped test specimens (30 mm length, 10 mm gauge length, 2.5 mm width and 2 mm thickness; based on the ASTM standard D3039 [25]) were printed using the mSLA 3D Printer. AnyCubic Photon Slicer software was used to set the orientation and to add necessary supports. Support material, consisting of six support fixtures per specimen, was added in the grip areas, and not along the gauge length, in order to avoid defects and damage to the specimens during removal from the print bed.

Tensile testing was performed using a Psylotech μTS mechanical testing frame (Psylotech Inc., Evanston, IL, USA) with a 1-kN windowing load cell. Strain measurement was conducted using microscope-enabled digital image correlation (DIC; Vic 2D 6, Correlated Solutions Inc., USA). A microscope (BXFM, Olympus Corp., Center Valley, PA, USA) with a digital camera (Point Grey, 5 MP, 2/3″ detector) was mounted over the test system to take magnified images of the gauge length during the test. A 2.5× magnification objective lens (Olympus Corp., Center Valley, PA, USA) was used. The resulting spatial resolution was 1450 pixels mm^{-1}.

Test specimens ($n = 7$ per group) were sprayed with high-resolution toner powder (Xerox Phaser 6000) by using an atomizer jar to create speckle patterns that enabled DIC analysis. The speckling particles were 4–5 μm in diameter. In displacement control mode, specimens were first preconditioned at 1 Hz for 100 cycles. Then extension was applied at the rate of 16 μm/s (average strain rate of 0.0016 s^{-1}). All testing was carried out at room temperature. Data were acquired at 5 Hz. The average engineering strains were measured from the DIC using a line extensometer tool. The engineering stress was calculated by dividing force by initial cross-sectional area. Elastic modulus was determined from the slope of the initial linear elastic portion (0–0.3% strain) of the stress–strain curve, respectively. Yield strength was calculated using the conventional 0.2% offset from the linear portion of the curve. Toughness values were obtained as the area under the stress-strain curves up to the point of fracture.

2.7. Single edge notch 3-point bending (SENB) testing

Single-point fracture toughness (K_{1c}) of the mSLA-printed nanocomposites was measured using the same testing frame equipped with a 3-point bending fixture and performed according to ASTM D5045-14 [26]. The SENB test specimens with length of 50 mm (gauge length 40 mm), thickness (B) of 5 mm and a width (W) of 10 mm were 3D printed similarly to the specimens for tensile testing (Section 2.6). A 4.5-mm notch was cut into the width by using an IsoMet^{tm} low-speed metallurgical saw (Buehler Ltd., IL, USA) and then a micro-crack was created by tapping the specimens gently with a sharp razor blade placed in the notch. The initial crack length (a_0) fell within the $0.45 < a/W < 0.55$ specification. All testing ($n = 6$) was conducted at room temperature and in displacement control mode with crosshead speed 3.3 μm/s. Data were acquired at 5 Hz.

2.8. Scanning electron microscopy (SEM) and fractography

SEM imaging was conducted using a Quanta FEG 250 (ThermoFisher Scientific, USA) in low vacuum mode. Images of the fracture surfaces after tensile and fracture tests were acquired by mounting the fractured specimens on SEM stubs vertically and without further treatment.

2.9. Swelling and hydrolytic degradation of nanocomposites

Water absorption and hydrolytic degradation of the 3D printed nanocomposites were evaluated by soaking in deionized (DI) water at 37 °C. Disc specimens (12 mm in diameter and 5 mm in thickness) were 3D printed using the same printing conditions as for tensile mechanical testing specimens (as described in Section 2.6). Incubation was performed for 1, 3, 7, 14 and 28 days. Each disc was weighed prior to incubation and this was recorded as the initial mass (m_i). After each time point, discs ($n = 5$) were removed from DI water and weighed immediately after gently wiping the surfaces. This wet mass is referred to as the swelled mass (m_s). Next, the discs were dried under reduced pressure for a week followed by drying in an oven at 60 °C for 24 h to more completely remove the absorbed water. Then the mass of the disc was recorded as final mass (m_f) and used to calculate the swelling and degradation of the nanocomposites by following the equations:

$$Swelling\ (gain\ of\ mass, \%) = \frac{m_s - m_f}{m_f} \times 100$$

$$Degradation\ (loss\ of\ mass, \%) = \frac{m_i - m_f}{m_i} \times 100$$

2.10. In vitro bioactivity of the 3D printed nanocomposites

The *in vitro* bioactivity was evaluated by studying the deposition of bone-mimetic apatite on the surfaces of the nanocomposite disc specimens (12 mm in diameter and 5 mm in thickness) by incubation in SBF. The specimens were 3D printed using methods similar to those described in Section 2.6. The SBF solution mimics the composition and concentration of the inorganic part of human blood plasma and was prepared as described elsewhere [27]. Each specimen was incubated at 37 °C with 20 mL of SBF in a polypropylene vial, tightly covered with a lid. The solution was replenished with fresh SBF solution every 48 h. After each time point, the discs were removed from the SBF solution, rinsed with DI water and dried under reduced pressure at room temperature for 24 h prior to SEM imaging. The imaging was conducted using a Quanta FEG 250 (ThermoFisher Scientific, USA) in low vacuum mode (similar to the

method given in Section 2.8). The gain of mass due to the apatite deposition was calculated by the following equation:

$$Gain\ of\ mass\ (\%) = \frac{m_f - m_i}{m_i} \times 100$$

2.11. Biodegradation in enzymatic and oxidative media

The degradation behavior of the 3D printed nanocomposites was evaluated by incubating discs (12 mm in diameter and 5 mm in thickness) in oxidative and enzyme degradation solutions at 37 °C for up to 28 days. The initial dry mass (m_i) was recorded prior to sterilization and incubation. The discs were sterilized in 70% ethanol (20 min), rinsed twice in PBS and blotted dry. Each disc was placed in 3 mL of either oxidative solution (20% H_2O_2 in water with 0.1 M $CoCl_2$), lipase solution (100 units of lipase from Thermomyces lanuginosus/mL of PBS), esterase solution (300 units of esterase from porcine liver/mL of PBS) or control solution (PBS) [28,29]. All solutions were prepared fresh from reagents obtained from Sigma-Aldrich and contained 0.02 wt% NaN_3, as a bactericide. All solutions were changed every 2 days. After 14 and 28 days, discs ($n = 3$ for each SP0, SP5 and SP10) were removed from solutions and weighed immediately after gently blotting of the surfaces. This is referred to wet mass (m_w). At the 28-day time-point, the discs were dried under reduced pressure for a week followed by drying in an oven at 60 °C for 24 h to completely remove water. Then the mass of the disc was recorded as final mass (m_f) and used to calculate the final degradation of the nanocomposites by following the equations:

$$Mass\ change, wet\ conditions\ (\%) = \frac{m_w - m_i}{m_i} \times 100$$

$$Final\ degradation, mass\ loss\ at\ day\ 28\ (\%) = \frac{m_i - m_f}{m_i} \times 100$$

2.12. Cell viability and proliferation assessment

2.12.1. Osteoblast cell culture

Mouse pre-osteoblast MC3T3-E1 (ATCC, Manassas, Virginia, USA) cells were differentiated to osteoblasts using an osteogenesis assay kit (MilliporeSigma, Oakville, Ontario, Canada). Differentiated MC3T3-E1 osteoblast-like cells were cultured in a growth medium composed of Minimum Essential Medium alpha (α-MEM) (Life technologies, Burlington, Ontario, Canada) supplemented with 10% fetal bovine serum (FBS), 1% penicillin/streptomycin (P/S), 0.2 mM ascorbic acid-2-phosphate and 10 mM β-glycerophosphate. Cells from passages 2 to 6 were used for the experiments.

2.12.2. Osteoblast attachment and proliferation on nanocomposite discs

3D printed nanocomposite discs (8 mm in diameter and 1 mm in thickness) were washed with 70% ethanol and phosphate buffered saline twice (5 min per wash) and further sterilized under UV light for 20 min. To improve cell adhesion, discs were incubated overnight at 37 °C (5% CO_2) in α-MEM supplemented with 50% FBS and 1% P/S. Commercially available sterile hydroxyapatite (HA) discs (8 mm in diameter and 2 mm in thickness, 3D Biotek, USA) were used as controls. To keep cells on the discs during seeding and incubation times, each disc was placed in a silicone ring (Dow Corning Silastic, HelixMark, USA) and then added to a well of a 24-well plate. Osteoblasts were seeded at a density of 10,000 cells per disc (20,000 cells/cm^2). Samples were incubated for 2 h to allow for cell attachment and 0.25 mL of growth medium (α-MEM supplemented with 10% FBS, 1% P/S, 0.2 mM ascorbic acid-2-phosphate and 10 mM β-glycerophosphate) was then added. Samples were cultured for 1, 3 and 7 days and medium was changed every day.

Cell proliferation after 1, 3- and 7-days of culture was characterized using XTT (sodium 3′-[1-(phenylaminocarbonyl)-3,4-tetrazolium]-bis (4-methoxy6-nitro) benzene sulfonic acid hydrate; TACS XTT cell proliferation kit, R&D Systems, Minneapolis, USA). XTT solution was added to each well and the samples were incubated for 2.5 h. The supernatant was then transferred to a 96-well plate and absorbance was measured at 490 nm with a reference wavelength of 630 nm on a SpectraMax Plus 384 Microplate Reader. Results are expressed as corrected absorbance values (*i.e.* subtracting working solution absorbance from sample absorbance).

Following XTT, live/dead staining (Life Technologies Inc., CA) was performed. The discs were incubated with a growth medium containing 2 μM Calcein AM (stains live cells green) and 4 μM EthD-1 (stains dead cells red) for 30 min at 37 °C, directly followed by imaging with a Nikon Eclipse TS100 fluorescence microscope (Tokyo, Japan).

2.13. Statistical analysis

Data are represented as mean ± standard deviation (SD). All data were analyzed using SigmaStat (Version 4.0, Systat Software Inc., CA, USA). Means were compared using one-way or two-way analysis of variance (ANOVA) followed by a Tukey's multiple comparison test. Differences between means were considered statistically significant at $p < 0.05$.

3. Results

3.1. Characterization of AESO/nHA/PEGDA nanocomposite inks

The UV doses required for successfully curing various layer thicknesses were determined by generating standard cure depth curves. Plots of the cured depths in response to different UV doses for the SP0, SP5, and SP10 nanocomposite inks are shown in Fig. S1A. Incorporation of nHA decreased the cure depth over the same dose range presumably due to the blocking and scattering of UV by the nHA particles. FTIR spectra (Fig. S1B) of all of the cured nanocomposites showed no peak at 1630 cm^{-1} (associated with stretching vibration for C═C) and a small peak at 806 cm^{-1} (for asymmetric vibration of out-of-plane vinyl groups) [5,13]. This indicates the minimal presence of unreacted monomers on the cured nanocomposites (4–9%, based on calculating the ratio of area under the C═C peaks after normalizing with C═O peak from FTIR spectra of cured and uncured specimens). Thermogravimetric analysis (TGA) was performed to confirm the ratio of nHA to AESO/PEGDA resin in the 3D printed nanocomposites (Fig. S2A). All nanocomposites burned in the 300 to 500 °C range. The remaining mass presumably corresponds to the inorganic nHA particles. The nHA volume fractions after burnout of SP0, SP5 and SP10 were calculated as 0%, 4.71 ± 0.12% and 8.97 ± 0.40%, respectively ($n = 3$). The DSC curves (Fig. S2B) for all the nanocomposites showed similar trends, and notably an absence of any detectable change in heat capacity, due to a glass transition or melting, within the examined temperature range.

3.2. Rheology and printability of nanocomposite inks

The viscosity increased upon addition of nHA powder to the AESO/PEGDA resin (Fig. 1A). Addition of 10 vol% of nHA (SP10) increased the viscosity from 0.2 to 0.49 Pa·s. All inks displayed Newtonian behavior with near-zero shear yield strength (Fig. 1B). The SP15 nanocomposite ink demonstrated a small shear yield strength (0.11 ± 0.04 Pa), and therefore, this SP15 ink was not carried forward for further analyses because shear yield strength can cause defects during mSLA. Indeed, the printability decreased as the nHA content was increased, presumably due to the blocking and scattering of UV by nanoparticles (Table 2) and due to changes in rheology. The printability number for SP10 was 0.45, decreased from 0.64 for SP0. These printability results are consistent with the cure-depth characteristics of nanocomposite inks.

A model of a human femoral diaphysis was printed using mSLA and SP5 nanocomposite ink (Fig. 2). This demonstrates the utility of the ink towards the additive manufacturing of meaningful scaffolds and synthetic grafts.

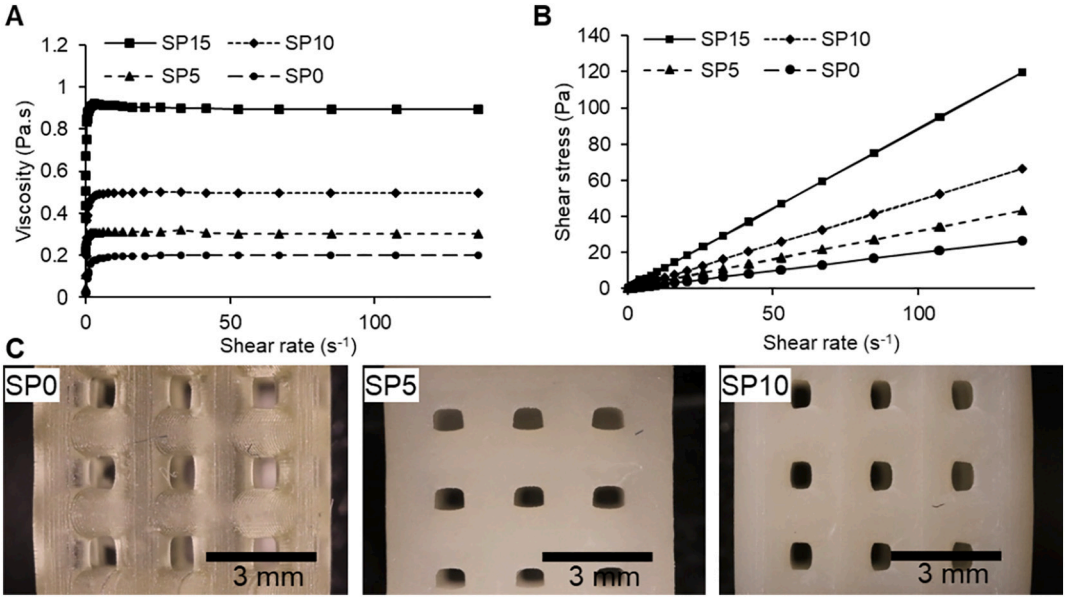

Fig. 1. Rheology and printability of the nanocomposite inks ($n = 3$). Representative plots of A) viscosity *vs* shear strain rate and B) shear stress *vs* shear rate. All nanocomposite inks were Newtonian and viscosity increased with increased nHA content. C) Representative digital images of 3D printed lattice cubes used to calculate printability of the inks.

Table 2
Viscosity, shear yield strength and printability results of as-prepared nanocomposite inks (n = 3; data are presented as mean ± SD).

Nanocomposites	Viscosity (Pa·s)	Shear yield strength (Pa)	Printability (Pr)
SP0	0.20 ± 0.00	0	0.64 ± 0.03
SP5	0.31 ± 0.01	0	0.53 ± 0.02
SP10	0.49 ± 0.01	0	0.45 ± 0.01
SP15	0.89 ± 0.01	0.11 ± 0.04	–

3.3. Mechanical properties of the printed nanocomposites

The mechanical properties of AESO/PEGDA/nHA nanocomposites were measured by tensile and fracture toughness testing. All specimens were printed using mSLA and tested according to ASTM standards (Fig. S3). The representative engineering stress *vs* engineering strain curves show that with increasing volume fraction (vol%) of nHA from 5 to 10%, the strength increased (Fig. 3A). The mean fracture strengths, Young's moduli, yield strengths, strains-at-fracture, toughnesses, and fracture toughnesses are summarized in Table 3. Both tensile fracture strength and modulus values were dramatically improved upon inclusion of 10 vol% nHA. SP10 demonstrated 30.8 ± 1.2 MPa for tensile strength (a 58% increase over SP0) and 1984.37 ± 126.72 MPa for modulus (144% increase over SP0). The yield strengths followed a similar trend. The AESO/PEGDA resin fractured at close to 12% strain in tension, whereas the SP10 nanocomposite fractured at ~7%, an expected reduction in ductility due to nanoparticle inclusion.

The representative load-displacement curves from SENB fracture testing indicate relatively brittle fracture of both the nanocomposites and the resin (Fig. 3B). Both SP5 and SP10 had significantly higher fracture toughness values (0.55 ± 0.02 and 0.58 ± 0.05 MPa·$m^{1/2}$, respectively) than the pure resin SP0 (0.41 ± 0.04 MPa·$m^{1/2}$). Interestingly, SP10 demonstrated some extent of stable tearing which shows that inclusion of higher amount of nHA enhanced its resistance to crack extension.

Fig. 4 presents SEM images of the fracture surfaces of 3D printed SP0, SP5 and SP10 nanocomposites after tensile testing. The flat fracture surfaces of SP0 indicate brittle fracture. SP5 nanocomposites showed wedges and rough surface after tensile fracture. The roughness of the fracture surfaces visually increased upon incorporation of higher amounts of nHA. Micro-scale agglomerates of nHA can be observed on the higher magnification images of SP5 and SP10 (Fig. 4E–F).

The SEM images of fracture surfaces after SENB fracture testing (Fig. 5) are consistent with those from the tensile testing. The fracture surface of SP0 was flat and smooth. On the other hand, the fracture surfaces of the 3D printed nanocomposites, SP5 and SP10, had rough

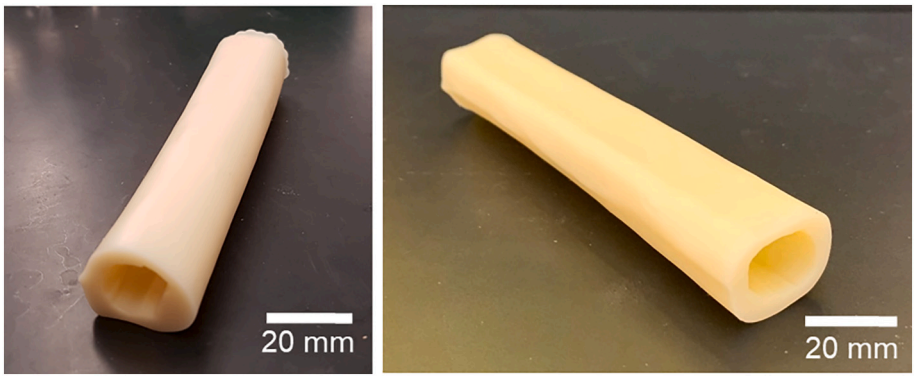

Fig. 2. mSLA printed human femoral diaphysis model using SP5 nanocomposite ink.

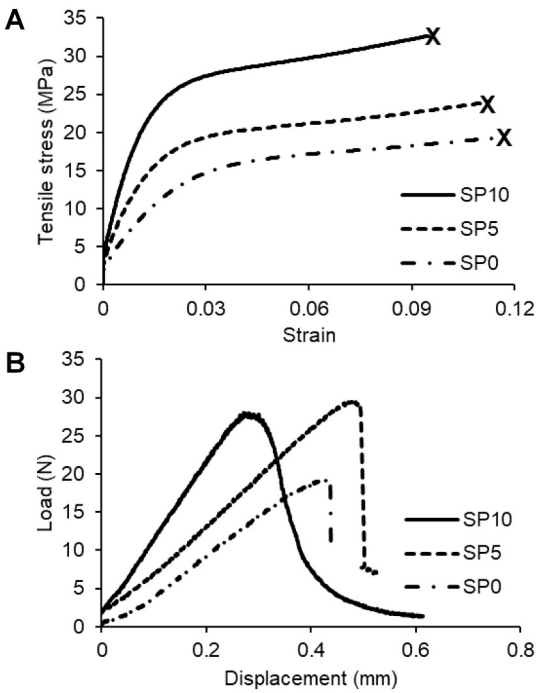

Fig. 3. Tensile and fracture mechanical testing of mSLA-based 3D printed nanocomposite dogbones and SENB beams, respectively. A) Representative stress – strain curves from tensile testing and B) representative load-displacement curves from SENB fracture testing.

wedge morphology in the fracture direction, indicative of tearing (black arrows). These rough morphologies of SP5 and SP10 may result from nHA incorporation and the interaction of nanoparticles with the polymer matrix.

3.4. Swelling and degradation

Excessive swelling in physiologic conditions may result in unexpected damage and instability of the biomaterial. We tested swelling behavior and hydrolytic degradation of our 3D printed nanocomposites to evaluate their initial stability *in vivo*. The nanocomposites and resin absorbed similar amounts of water (Fig. 6A). Approximately 3 wt% water absorption indicates neither hydrophobicity nor excessive swelling. The nanocomposites reached equilibrium with water within 10 days of immersion. The incorporation of nHA did not affect the swelling detectably.

Hydrolytic degradation of the nanocomposites was negligible (~0.3%) (Fig. 6B). However, SP5 and SP10 lost more mass than SP0 (not statistically significant) when incubated in DI water for 1 day to 4 weeks. This loss occurred within the first day of incubation and may have been the result of an initial loss of nHA from the surface.

3.5. In vitro surface mineralization

When incubated in SBF, the 3D printed resin and nanocomposites underwent extensive apatite deposition within 7 days (Fig. 7B). The nanocomposites lost mass up to 2 weeks of incubation presumably due to the degradation discussed in Section 3.4. The mass gain plotted in Fig. 7A represents the balance of mass loss due to the degradation and mass gain due to the deposition of apatite. The formation of crystalline biomimetic apatite on the surface of SP0, SP5 and SP10 suggests excellent bone-bioactivity potential.

3.6. Biodegradation in enzymatic and oxidative media

In agreement with observations from the swelling and hydrolytic degradation study in Section 3.4, there was a small non-statistically significant swelling (2 to 3%) of the SP0, SP5 and SP10 discs in the lipase and esterase degradation solutions (Table 4) while slightly higher swelling occurred under oxidative conditions. A 1 to 2% mass loss was observed for samples incubated in the oxidative solution containing $CoCl_2$ (acting as a Fenton's reagent to provide a stronger oxidizing medium [30]). Overall, no significant biodegradation was observed at day 28 (around 1% loss in mass), suggesting limited bulk enzymatic and oxidative degradation of the nHA nanocomposites.

3.7. Differentiated MC3T3-E1 osteoblasts proliferation and viability on nanocomposite discs

Cell proliferation and viability on the three nanocomposites were assessed after 1, 3, and 7 days of culture. As shown in Fig. 8A, differentiated MC3T3-E1 osteoblasts showed excellent viability on SP0, SP5, and SP10 surfaces at all time-points. A few dead cells were observed. Cells seeded on SP5 and SP10 demonstrated excellent morphology at day 1. While a higher cell density could be observed on SP0 compared to SP5, SP10 and HA discs after day 1, a significant increase in proliferation ($p < 0.05$) was only observed on SP5, SP10 and HA discs at day 3 and day 7 (Fig. 8B). The two-way ANOVA revealed a statistically significant interaction between nanocomposite groups ($p = 0.018$) and between nanocomposite groups and days ($p = 0.004$). Furthermore, the XTT results combined with the live/dead staining suggest increased osteoblast viability and proliferation with increased nHA content in the nanocomposites.

4. Discussion

mSLA 3D printing has the ability to improve the fabrication of complex structural grafts for bone regeneration and reconstruction. However, this requires suitable biomaterial inks that once printed have competent mechanical properties and biocompatibility to enhance bone regeneration. In this work, we studied the effect of nHA content on the viscosity and printability of AESO/nHA/PEGDA nanocomposites, and successfully printed test specimens and objects by using mSLA technique. nHA is a bone-bioactive component and widely studied *in vitro* and *in vivo* for its bioactivity and osteoconductivity [14,15]. Our results support the hypothesis that the addition of nHA to the AESO/PEGDA resin would improve the mechanical properties, cytocompatibility, and bioactivity of the 3D printed nanocomposites. We measured the tensile and fracture mechanical properties, water absorption, and hydrolytic, enzymatic and oxidative biodegradation *in vitro* of these 3D printed nanocomposites. Bone-bioactivity and cytocompatibility of the nanocomposites were evaluated by apatite deposition in SBF and studying the adhesion and proliferation of osteoblasts on the nanocomposite surfaces.

For successful 3D printing of bone tissue engineering grafts, most of

Table 3
Tensile and fracture test data for the 3D printed AESO/nHA/PEGDA nanocomposites. Data are presented as mean ± SD ($n = 7$ specimens for tensile tests and $n = 6$ for fracture tests of each composition). Different lower-case letters (a, b, c) indicate statistically significant differences at $p < 0.05$.

	Tensile fracture strength (MPa)	Modulus (MPa)	Yield strength (MPa)	Strain at fracture (%)	Toughness (MPa)	Fracture toughness (MPa·m$^{1/2}$)
SP0	19.5 ± 1.4^{a}	815 ± 94^{a}	11.3 ± 1.0^{a}	11.8 ± 2.5^{a}	1.86 ± 0.50^{a}	0.43 ± 0.04^{a}
SP5	21.5 ± 2.0^{a}	1043 ± 203^{b}	12.7 ± 1.4^{a}	10.1 ± 0.9^{ab}	1.75 ± 0.36^{a}	0.55 ± 0.02^{b}
SP10	30.8 ± 1.2^{b}	1984 ± 127^{c}	21.4 ± 0.4^{b}	7.3 ± 1.3^{b}	1.87 ± 0.40^{a}	0.58 ± 0.05^{b}

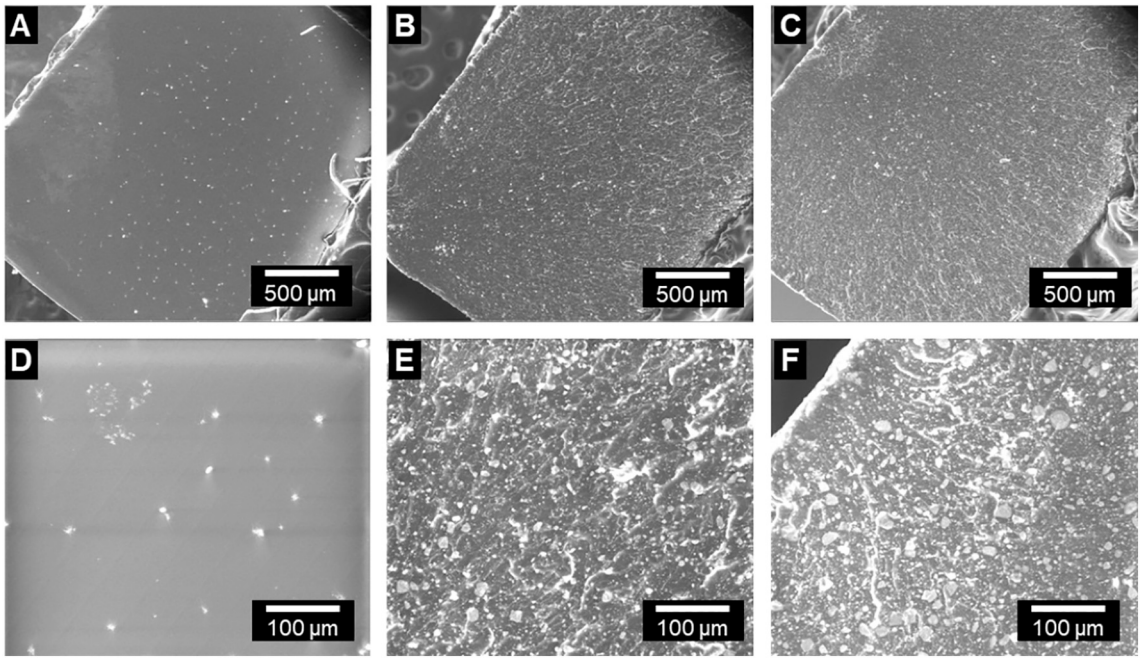

Fig. 4. Representative SEM images of fracture surfaces from tensile mechanical testing. Panels A–C are low magnification images and panels D–F are higher magnification images. A, D) SP0, B, E) SP5 and C, F) SP10. White specks on the surfaces are residual carbon particles from the DIC strain measurement during the tensile testing.

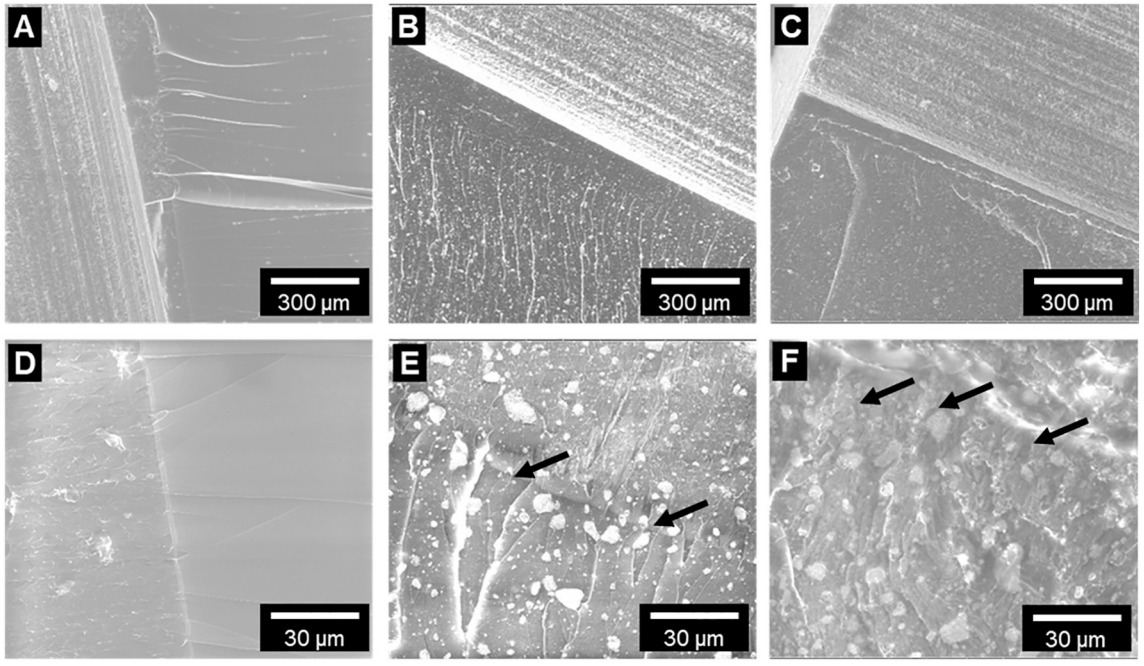

Fig. 5. Representative SEM images of fracture surfaces from SENB fracture testing. Panels A–C are low magnification images and panels D–F are higher magnification images. A, D) SP0, B, E) SP5 and C, F) SP10. Black arrows in panels E and F indicate the rough wedge morphology oriented in the crack propagation direction.

the nanocomposite biomaterial inks developed and reported in the literature thus far are focused on fabricating porous scaffolds *via* fused deposition modeling (or liquid deposition modeling) and extrusion-based 3D printing (or direct ink writing) [31,32]. These methods of 3D printing can print viscous nanocomposite inks but the part-infidelity or inconsistency generated during fabrication process due to the nozzle clogging and/or inhomogeneous dispersion of nanoparticles may lead to reduced strength and rapid degradation [33–35]. Moreover, these techniques are time-consuming and arduous. mSLA, on the other hand, is fast and can print parts with high resolution that are nearly defect-free. The rheological properties of our nanocomposite inks are favorable for successful and efficient mSLA printing of complex microstructures. To our knowledge, there are no studies in the available literature on mSLA-based 3D printing of nanocomposite grafts for reconstruction of load-bearing bone defects.

Most SLA printed biomaterials are limited to one or a blend of multiple bioactive polymers-based resins, due to the viscosity threshold for mSLA printing. Few studies to date have shown incorporation of

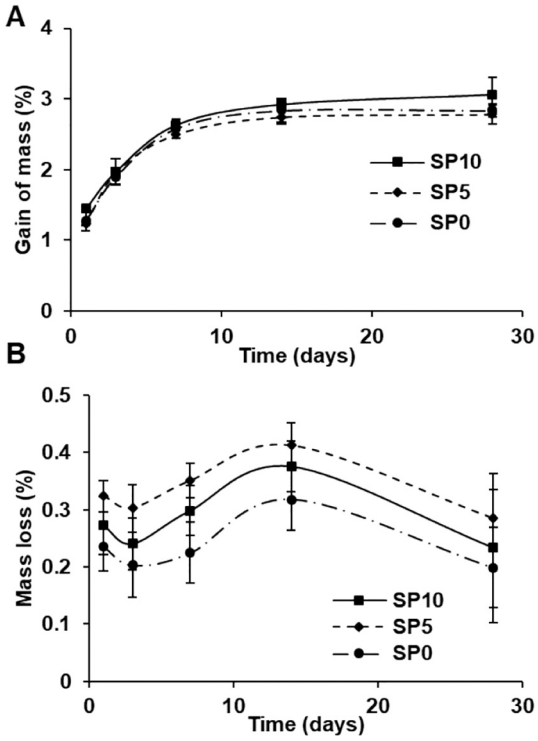

Fig. 6. Swelling (water absorption) and hydrolytic degradation of the nanocomposites after immersion and incubation in deionized water. A) Gain of mass due to swelling in deionized water, and B) mass loss due to hydrolytic degradation. Results are reported as mean ± SD (n = 5). None of the means were statistically different.

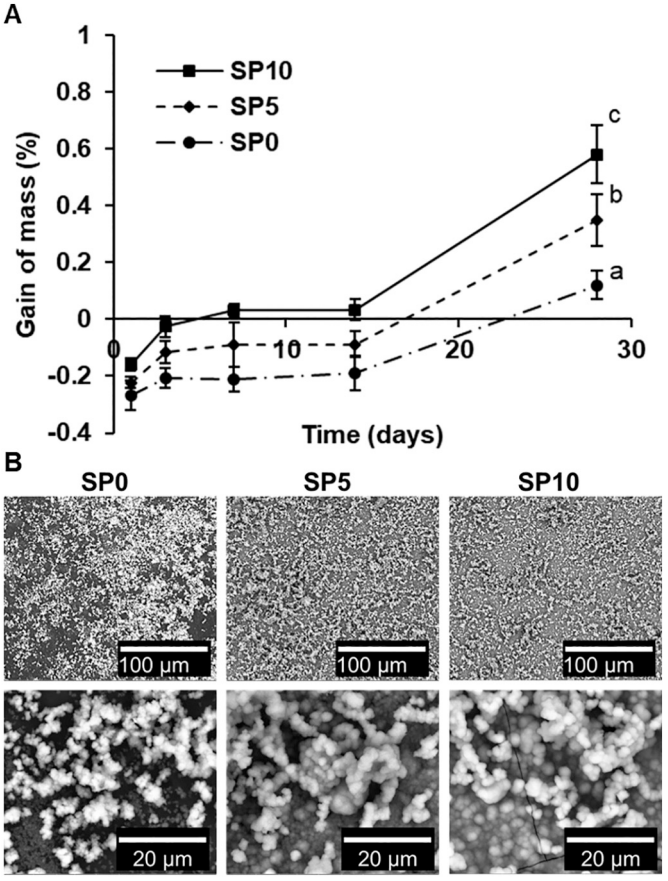

Fig. 7. Biomineralization on 3D printed nanocomposite discs. A) Change of mass after incubation in SBF at various time points. Data are presented as mean ± SD (n = 5). Different lower case letters indicate that the means are statistically significant at $p < 0.05$. B) Representative SEM images of apatite deposited onto disc surfaces after 28 days of incubation. Low magnification images in the upper row and high magnification images in the bottom row.

hydroxyapatite with polymer blends and their successful 3D printing using either SLA or DLP [36–40]. The focus of these previous studies was to fabricate porous scaffolds for bone tissue engineering. In some of these studies, the polymers were used as binder for the accompanied ceramics and burnt out in a final stage to fabricate porous ceramic-only scaffolds. Burn-out and sintering caused micron-scale crack formation in the scaffolds and weakened their mechanical properties [37,39,40]. Although the reported mechanical properties of these 3D printed scaffolds were compatible with human trabecular bone, none of these materials would be eligible for load bearing skeletal reconstructions. Moreover, porous microstructure with higher surface area-to-volume ratio assists faster degradation or dissolution *in vivo*, which results in rapid loss of the scaffold materials and poses a major challenge in matching the rate of natural bone formation or remodeling through cell-mediated resorption. For successful bone regeneration through natural bone remodeling processes, it is important to mimic the organic-inorganic microstructure of natural bone (such as allograft) which is osteogenic, slow to degrade, mechanically competent and stable [44–46].

Addition of 10 vol% of nHA (SP10 nanocomposite) sharply increased the tensile strength (58%), yield strength (90%), Young's modulus (144%) and plane-strain fracture toughness (41%) compared to the pure AESO/PEGDA resin. The increase in mechanical strength is directly attributed to the nanoscale load transfer between phases partially due to interactions facilitated by the high surface area-to-volume ratio. This reinforcement behavior greatly depends on the volume fraction, distribution and dispersion of nHA in the polymer matrices. However, the SEM imaging of the fracture surfaces of the nanocomposite specimens after tensile and fracture testing revealed micron-sized agglomerates. This suggests that the dispersion of nHA must be further improved to further increase the strength of AESO/nHA/PEGDA nanocomposites. In addition, the mechanical properties of SP10 are not comparable to those of human cortical bone. For example, the tensile strength and modulus of human cortical bone are 135 ± 15 MPa and 19.8 ± 1.8 GPa, respectively [47,48], while the tensile fracture stress and modulus of SP10 is 31 ± 1 MPa and 2.0 ± 0.1 GPa, respectively. It has been reported that the human tibia [49] or femur [50] may experience principal strain (tensile) during walking or running in the range of 500–1000 με. By considering the elastic modulus of cortical bone (~20 GPa), this strain

Table 4
Change in mass of nanocomposites over 28 days of incubation in various degradation media. Data are presented as mean ± SD (n = 3). None of the nanocomposites showed statistically significant mass loss ($p > 0.05$) when incubated in PBS, lipase, esterase and oxidative media.

Degradation medium	Nanocomposites	Day 14 Wet mass change (%)	Day 28 Wet mass change (%)	Day 28 Dry mass change (%)
PBS	SP0	2.1 ± 0.1	2.2 ± 0.1	−0.4 ± 0.1
	SP5	2.0 ± 0.1	2.1 ± 0.1	−0.3 ± 0.1
	SP10	2.2 ± 0.1	2.3 ± 0.1	−0.1 ± 0.1
Lipase (100 U/mL)	SP0	2.2 ± 0.1	2.4 ± 0.1	−0.2 ± 0.1
	SP5	2.1 ± 0.1	2.3 ± 0.1	−0.1 ± 0.1
	SP10	2.3 ± 0.1	2.5 ± 0.1	0.0 ± 0.1
Esterase (300 U/mL)	SP0	2.4 ± 0.1	2.7 ± 0.1	−0.1 ± 0.1
	SP5	2.3 ± 0.1	2.5 ± 0.1	0.0 ± 0.1
	SP10	2.5 ± 0.1	2.8 ± 0.1	0.2 ± 0.1
H_2O_2 (20%) with $CoCl_2$	SP0	2.1 ± 0.1	1.6 ± 0.1	−1.3 ± 0.1
	SP5	1.3 ± 0.1	0.01 ± 0.01	−2.1 ± 0.1
	SP10	1.8 ± 0.1	1.3 ± 0.1	−1.0 ± 0.1

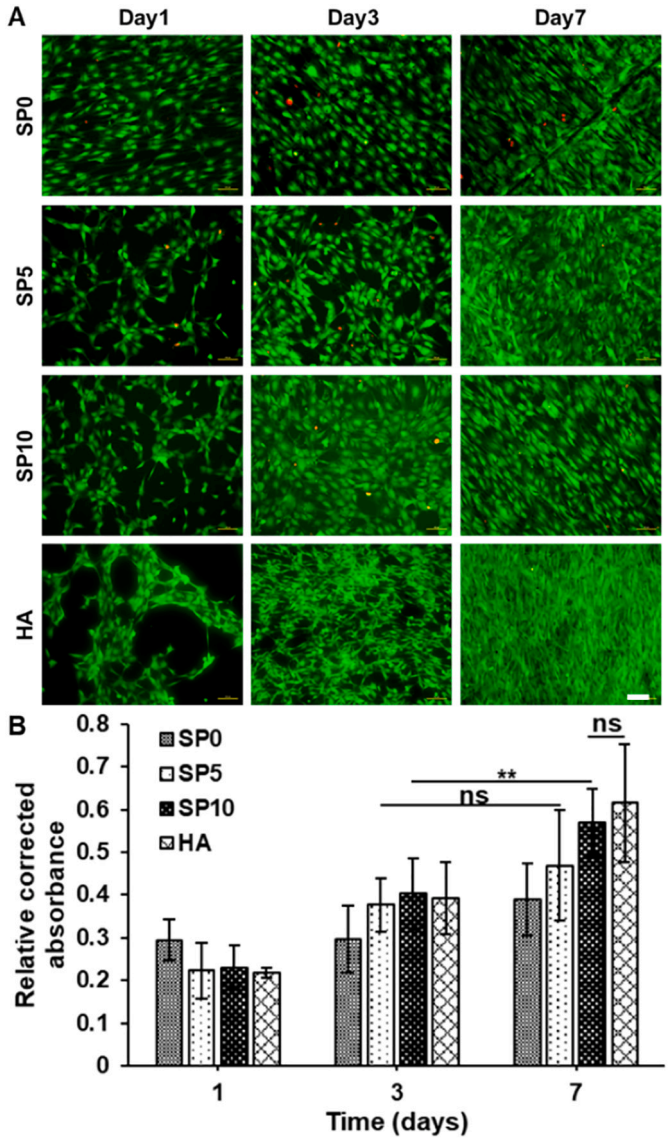

Fig. 8. Differentiated MC3T3-E1 osteoblast cell viability, adhesion and proliferation on 3D printed nanocomposite discs. A) Representative images of live/dead staining of cells on SP0, SP5, SP10, and HA discs at day 1, 3 and 7 days after seeding. Calcein AM stains live cells green, and EthD-1 stains dead cells red. Scale bar represents 100 μm. B) Proliferation of osteoblast cells as measured by XTT assay. Data are means ± SD ($n = 7$ for nanocomposite discs and $n = 4$ for HA discs, from 3 experiments). (For interpretation of the references to color in this figure legend, the reader is referred to the web version of this article.)

may result from 10 to 20 MPa of stress, which is lower than the ultimate tensile stress of SP10 nanocomposite. Moreover, commercially available poly-methylmethacrylate (PMMA)-based bone cements, which have been widely used in clinics over the last 60 years but are bio-inert and cause severe necrosis to host tissue during implementation, have tensile strengths and moduli of 30–50 MPa and 2.4–3.2 GPa, respectively [51–53]. The tensile mechanical properties of our SP10 nanocomposite are thus comparable with these commercially available bone cements. The SP10 demonstrated stable tearing during the fracture tests, which indicates sub-micron-scale crack deflection and toughening effects of nHA particles dispersed and embedded in the AESO/PEGDA matrix. Although the fracture toughness of SP10 (0.58 ± 0.05 MPa·m$^{1/2}$) is not comparable with human cortical bone (2–8 MPa·m$^{1/2}$) [54], it is close to the fracture toughness of poly(methylmethacrylate)-based bone cements (0.88–1.6 MPa·m$^{1/2}$) [55,56]. Importantly, our prints have much fewer and smaller defects than typical PMMA bone cements, and therefore the lower fracture toughness is not considered critical. Improvement of the mechanical properties may be achieved in the future by addition of greater amounts of nHA following optimization of the rheological properties of the resin.

In previous work by others, nHA-poly(ester urethane)-based nanocomposites with high nHA content (~30 vol%) were developed [46,57]. The compressive strength (70–90 MPa), bone bioactivity and degradation of these nanocomposites were compatible with natural bone. However, these nanocomposites were putty-like, settable bone cements, and as such, they are not suitable for 3D printing. It is not possible to fabricate these previously published nanocomposites into complex microstructure to match patient-specific and defect-specific geometries.

Hydroxyapatite undergoes solution-mediated dissolution but its low solubility leads to very slow degradation; this can promote cell-mediated resorption [58,59]. The dissolution of nHA from nanocomposites largely depends on the degradation behavior of embedding matrices. Slow and controllable degradation is crucial to maintaining initial stability of the grafts and to ensure the recruiting and homing of osteoprogenitor cells [60]. An ideal bone graft should degrade slowly and controllably, and even more appropriately through osteoclast-mediated resorption to assist the natural bone remodeling process. The *in vivo* degradation behavior of implantable biomaterials can be assessed by several pathways, such as hydrolytic, oxidative, and enzymatic degradation *in vitro* [61–63]. Polymers degrade by hydrolytic pathways as water molecules react with the polymer backbone and scission sites lead to smaller chains until they become small molecules and are excreted from the body [61,62]. Several enzymes present in serum or produced by macrophages and osteoclasts, such as proteases or esterases, can react with polymer chains or functional groups and the degradation process results in small oligomers [28,63–65]. Oxidative degradation is a well-studied degradation process, especially for biomaterials for bone and dental implants, in which reactive oxygen species, such as hydrogen peroxide (H_2O_2), nitric oxide (NO), hydroxyl radical ($^{\bullet}OH$) and the superoxide anion ($^{\bullet}O_2^-$) that are secreted by macrophages, neutrophils and giant cells, can react with the polymer chains [28,61,62]. PEGDA and copolymer of AESO/PEGDA have previously been tested for their biodegradation in lipase solution and demonstrated no mass loss after incubation for 24 days [66]. However, to our knowledge, there is no study on biodegradation of AESO/nHA/PEGDA nanocomposites in presence of esterase or under hydrolytic and oxidative conditions. Esters present in triglycerides and acrylate may be degraded by hydrolytic, esterase or oxidative pathways [29,62,67]. However, the 3D printed AESO/nHA/PEGDA nanocomposites in this study did not demonstrate excessive swelling and hydrolytic, enzymatic or oxidative degradation. These results suggest chemical and mechanical stability of 3D printed AESO/nHA/PEGDA nanocomposite grafts *in vivo* during early stages of healing.

Predicting a biomaterial's *in vivo* bone bioactivity is often evaluated by studying apatite deposition on the biomaterials surfaces after incubating in SBF *in vitro* [27]. The amount of deposited apatite indirectly predicts the bone-bonding ability of the biomaterials with native bone. Our nanocomposites have shown excellent apatite deposition after 28 days of incubation, and the amount of deposited apatite is directly proportional to the nHA content in the nanocomposites. Similar results were obtained with viability and proliferation of differentiated MC3T3-E1 osteoblasts whereby, as nHA content increased, increased viability and proliferation were observed. This is in agreement with previous work by Cai et al. who observed that nHA promoted MC3T3-E1 cell attachment, proliferation, and differentiation on nanocomposites of photo-crosslinked poly(ε-caprolactone) diacrylate with nHA [68]. No statistically significant difference was observed between SP10, our nanocomposite with the highest nHA content, and the HA control (100% HA), further highlighting the strong biocompatibility potential of the nanocomposite.

5. Conclusion

This study demonstrates that bioactive hydroxyapatite nanoparticles can be composited with novel AESO/PEGDA-based polymer matrices at moderate volume fractions (5 and 10%) and 3D printed using the mSLA technique. Confirming our hypothesis, the addition of nHA to the AESO/PEGDA resin improved the strength, fracture toughness, elastic modulus, osteoblast cytocompatibility, and bioactivity of the mSLA-printed nanocomposites. Furthermore, swelling and degradation were minimal in hydrolytic, enzymatic and oxidative degradation media. These findings emphasize the potential of mSLA-printed AESO/PEGDA/nHA nanocomposites as durable and cytocompatible graft materials for repair and reconstructions of load-bearing bone defects.

CRediT authorship contribution statement

Dibakar Mondal: Conceptualization, Methodology, Validation, Formal Analysis, Investigation, Data Curation, Writing – Original Draft, Visualization

Zahra Haghpanah: Methodology, Validation, Formal Analysis, Investigation, Writing - Review & Editing, Visualization

Connor Huxman: Investigation

Sophie Tanter: Investigation

Duo Sun: Investigation

Maud Gorbet: Conceptualization, Methodology, Resources, Data Curation, Writing – Review & Editing, Supervision, Project Administration, Funding Acquisition

Thomas Willett: Conceptualization, Methodology, Resources, Data Curation, Writing – Review & Editing, Supervision, Project Administration, Funding Acquisition

Declaration of competing interest

The authors declare that they have no known competing financial interests or personal relationships that could have appeared to influence the work reported in this paper.

Acknowledgements

This work was supported by the Canadian Institutes of Health Research, Canada Foundation for Innovation, the Ontario Research Fund, and the University of Waterloo's Engineering Research Initiatives. ZH received support from the Natural Sciences & Engineering Research Council's CREATE training program in Global Biomedical Technology Research and Innovation at the University of Waterloo.

Appendix A. Supplementary data

Supplementary data to this article can be found online at https://doi.org/10.1016/j.msec.2021.112456.

References

[1] C. Mandrycky, Z. Wang, K. Kim, D.-H. Kim, 3D bioprinting for engineering complex tissues, Biotechnol. Adv. 34 (2016) 422–434, https://doi.org/10.1016/j.biotechadv.2015.12.011.

[2] J.W. Stansbury, M.J. Idacavage, 3D printing with polymers: challenges among expanding options and opportunities, Dent. Mater. 32 (2016) 54–64, https://doi.org/10.1016/j.dental.2015.09.018.

[3] F. Obregon, C. Vaquette, S. Ivanovski, D.W. Hutmacher, L.E. Bertassoni, Three-dimensional bioprinting for regenerative dentistry and craniofacial tissue engineering, J. Dent. Res. 94 (2015) 143S–152S, https://doi.org/10.1177/0022034515588885.

[4] H.-W. Kang, S.J. Lee, I.K. Ko, C. Kengla, J.J. Yoo, A. Atala, A 3D bioprinting system to produce human-scale tissue constructs with structural integrity, Nat. Biotechnol. 34 (2016) 312–319, https://doi.org/10.1038/nbt.3413.

[5] H.N. Chia, B.M. Wu, Recent advances in 3D printing of biomaterials, J. Biol. Eng. 9 (2015) 4, https://doi.org/10.1186/s13036-015-0001-4.

[6] S.C. Ligon, R. Liska, J. Stampfl, M. Gurr, R. Mülhaupt, Polymers for 3D printing and customized additive manufacturing, Chem. Rev. 117 (2017) 10212–10290, https://doi.org/10.1021/acs.chemrev.7b00074.

[7] I. Gibson, D. Rosen, B. Stucker, M. Khorasani, in: I. Gibson, D. Rosen, B. Stucker, M. Khorasani (Eds.), Introduction and Basic Principles, Addit. Manuf. Technol., Springer International Publishing, Cham, 2021, pp. 1–21, https://doi.org/10.1007/978-3-030-56127-7_1.

[8] S. Bose, S. Vahabzadeh, A. Bandyopadhyay, Bone tissue engineering using 3D printing, Mater. Today 16 (2013) 496–504, https://doi.org/10.1016/j.mattod.2013.11.017.

[9] J. Winder, R. Bibb, Medical rapid prototyping technologies: state of the art and current limitations for application in oral and maxillofacial surgery, J. Oral Maxillofac. Surg. 63 (2005) 1006–1015, https://doi.org/10.1016/j.joms.2005.03.016.

[10] L. Vidal, C. Kampleitner, M.Á. Brennan, A. Hoornaert, P. Layrolle, Reconstruction of large skeletal defects: current clinical therapeutic strategies and future directions using 3D printing, Front. Bioeng. Biotechnol. 8 (2020) 61. https://www.frontiersin.org/article/10.3389/fbioe.2020.00061.

[11] S. Miao, W. Zhu, N.J. Castro, M. Nowicki, X. Zhou, H. Cui, J.P. Fisher, L.G. Zhang, 4D printing smart biomedical scaffolds with novel soybean oil epoxidized acrylate, Sci. Rep. 6 (2016) 27226, https://doi.org/10.1038/srep27226.

[12] L. Bao, L. Bian, M. Zhao, J. Lei, J. Wang, Synthesis and self-assembly behavior of a biodegradable and sustainable soybean oil-based copolymer nanomicelle, Nanoscale Res. Lett. 9 (2014) 391, https://doi.org/10.1186/1556-276X-9-391.

[13] D. Behera, A.K. Banthia, Synthesis, characterization, and kinetics study of thermal decomposition of epoxidized soybean oil acrylate, J. Appl. Polym. Sci. 109 (2008) 2583–2590, https://doi.org/10.1002/app.28350.

[14] A.L. Rosa, M.M. Beloti, P.T. Oliveira, R. Van Noort, Osseointegration and osseoconductivity of hydroxyapatite of different microporosities, J. Mater. Sci. Mater. Med. 13 (2002) 1071–1075, https://doi.org/10.1023/A:1020305008042.

[15] J.D. de Bruijn, C.P.A.T. Klein, K. de Groot, C.A. van Blitterswijk, The ultrastructure of the bone-hydroxyapatite interface in vitro, J. Biomed. Mater. Res. 26 (1992) 1365–1382, https://doi.org/10.1002/jbm.820261008.

[16] T.J. Webster, C. Ergun, R.H. Doremus, R.W. Siegel, R. Bizios, Enhanced functions of osteoblasts on nanophase ceramics, Biomaterials. 21 (2000) 1803–1810, https://doi.org/10.1016/S0142-9612(00)00075-2.

[17] G. Gonzalez, A. Chiappone, I. Roppolo, E. Fantino, V. Bertana, F. Perrucci, L. Scaltrito, F. Pirri, M. Sangermano, Development of 3D printable formulations containing CNT with enhanced electrical properties, Polymer (Guildf.) 109 (2017) 246–253, https://doi.org/10.1016/j.polymer.2016.12.051.

[18] Q. Mu, L. Wang, C.K. Dunn, X. Kuang, F. Duan, Z. Zhang, H.J. Qi, T. Wang, Digital light processing 3D printing of conductive complex structures, Addit. Manuf. 18 (2017) 74–83, https://doi.org/10.1016/j.addma.2017.08.011.

[19] A. Bahmani, P.A. Comeau, J. Montesano, T.L. Willett, Extrudable hydroxyapatite/plant oil-based biopolymer nanocomposites for biomedical applications: mechanical testing and modeling, Mater. Des. 174 (2019), 107790, https://doi.org/10.1016/j.matdes.2019.107790.

[20] D. Mondal, A. Srinivasan, P. Comeau, Y.-C. Toh, T.L. Willett, Acrylated epoxidized soybean oil/hydroxyapatite-based nanocomposite scaffolds prepared by additive manufacturing for bone tissue engineering, Mater. Sci. Eng. C 118 (2021), 111400, https://doi.org/10.1016/j.msec.2020.111400.

[21] D. Mondal, T.L. Willett, Mechanical properties of nanocomposite biomaterials improved by extrusion during direct ink writing, J. Mech. Behav. Biomed. Mater. 104 (2020), 103653, https://doi.org/10.1016/j.jmbbm.2020.103653.

[22] P. Comeau, T. Willett, Impact of side chain polarity on non-stoichiometric nano-hydroxyapatite surface functionalization with amino acids, Sci. Rep. 8 (2018) 12700, https://doi.org/10.1038/s41598-018-31058-5.

[23] P. Comeau, T. Willett, Printability of methacrylated gelatin upon inclusion of a chloride salt and hydroxyapatite nano-particles, Macromol. Mater. Eng. 304 (2019), 1900142, https://doi.org/10.1002/mame.201900142.

[24] J.H. Lee, R.K. Prud'homme, I.a. Aksay, Cure depth in photopolymerization: experiments and theory, J. Mater. Res. 16 (2001) 3536–3544, https://doi.org/10.1557/JMR.2001.0485.

[25] Standard Test Method for Tensile Properties of Polymer Matrix Composite Materials, (n.d.).

[26] ASTM D5045 - 14 Standard Test Methods for Plane-Strain Fracture Toughness and Strain Energy Release Rate of Plastic Materials, n.d. https://www.astm.org/Standards/D5045.htm. (Accessed 22 February 2021).

[27] T. Kokubo, H. Takadama, How useful is SBF in predicting in vivo bone bioactivity? Biomaterials. 27 (2006) 2907–2915, https://doi.org/10.1016/j.biomaterials.2006.01.017.

[28] Y. Li, G.A. Thouas, H. Shi, Q. Chen, Enzymatic and oxidative degradation of poly (polyol sebacate), J. Biomater. Appl. 28 (2013) 1138–1150, https://doi.org/10.1177/0885328213499195.

[29] M.C.P. Brugmans, S.H.M. Söntjens, M.A.J. Cox, A. Nandakumar, A.W. Bosman, T. Mes, H.M. Janssen, C.V.C. Bouten, F.P.T. Baaijens, A. Driessen-Mol, Hydrolytic and oxidative degradation of electrospun supramolecular biomaterials: in vitro degradation pathways, Acta Biomater. 27 (2015) 21–31, https://doi.org/10.1016/j.actbio.2015.08.034.

[30] S.A.M. Ali, P.J. Doherty, D.F. Williams, Mechanisms of polymer degradation in implantable devices. 2. Poly(DL-lactic acid), J. Biomed. Mater. Res. 27 (1993) 1409–1418, https://doi.org/10.1002/jbm.820271108.

[31] Y. Wen, S. Xun, M. Haoye, S. Baichuan, C. Peng, L. Xuejian, Z. Kaihong, Y. Xuan, P. Jiang, L. Shibi, 3D printed porous ceramic scaffolds for bone tissue engineering: a review, Biomater. Sci. 5 (2017) 1690–1698, https://doi.org/10.1039/C7BM00315C.

[32] A.D. Valino, J.R.C. Dizon, A.H. Espera, Q. Chen, J. Messman, R.C. Advincula, Advances in 3D printing of thermoplastic polymer composites and nanocomposites, Prog. Polym. Sci. 98 (2019), 101162, https://doi.org/10.1016/j.progpolymsci.2019.101162.
[33] B.P. Croom, A. Abbott, J.W. Kemp, L. Rueschhoff, L. Smieska, A. Woll, S. Stoupin, H. Koerner, Mechanics of nozzle clogging during direct ink writing of fiber-reinforced composites, Addit. Manuf. 37 (2021), 101701, https://doi.org/10.1016/j.addma.2020.101701.
[34] X. Wang, M. Jiang, Z. Zhou, J. Gou, D. Hui, 3D printing of polymer matrix composites: a review and prospective, Compos. Part B Eng. 110 (2017) 442–458, https://doi.org/10.1016/j.compositesb.2016.11.034.
[35] C. Duty, C. Ajinjeru, V. Kishore, B. Compton, N. Hmeidat, X. Chen, P. Liu, A. A. Hassen, J. Lindahl, V. Kunc, What makes a material printable? A viscoelastic model for extrusion-based 3D printing of polymers, J. Manuf. Process. 35 (2018) 526–537, https://doi.org/10.1016/j.jmapro.2018.08.008.
[36] L. Gong, J. Li, J. Zhang, Z. Pan, Y. Liu, F. Zhou, Y. Hong, Y. Hu, Y. Gu, H. Ouyang, X. Zou, S. Zhang, An interleukin-4-loaded bi-layer 3D printed scaffold promotes osteochondral regeneration, Acta Biomater. 117 (2020) 246–260, https://doi.org/10.1016/j.actbio.2020.09.039.
[37] J. Zhang, D. Huang, S. Liu, X. Dong, Y. Li, H. Zhang, Z. Yang, Q. Su, W. Huang, W. Zheng, W. Zhou, Zirconia toughened hydroxyapatite biocomposite formed by a DLP 3D printing process for potential bone tissue engineering, Mater. Sci. Eng. C 105 (2019), 110054, https://doi.org/10.1016/j.msec.2019.110054.
[38] Y. Wu, X. Chen, G. Zhao, R. Chen, Y. Liu, H. Ren, X. Qu, Y. Liu, β-Tricalcium phosphate/ε-polycaprolactone composite scaffolds with a controllable gradient: fabrication and characterization, Ceram. Int. 45 (2019) 16188–16194, https://doi.org/10.1016/j.ceramint.2019.05.140.
[39] Z. Wang, C. Huang, J. Wang, B. Zou, Development of a novel aqueous hydroxyapatite suspension for stereolithography applied to bone tissue engineering, Ceram. Int. 45 (2019) 3902–3909, https://doi.org/10.1016/j.ceramint.2018.11.063.
[40] Y. Zeng, Y. Yan, H. Yan, C. Liu, P. Li, P. Dong, Y. Zhao, J. Chen, 3D printing of hydroxyapatite scaffolds withgood mechanical and biocompatible properties by digital light processing, J. Mater. Sci. 53 (2018) 6291–6301, https://doi.org/10.1007/s10853-018-1992-2.
[44] J.E. Dumas, E.M. Prieto, K.J. Zienkiewicz, T. Guda, J.C. Wenke, J. Bible, G.E. Holt, S.A. Guelcher, Balancing the rates of new bone formation and polymer degradation enhances healing of weight-bearing allograft/polyurethane composites in rabbit femoral defects, Tissue Eng. Part A 20 (2013) 115–129, https://doi.org/10.1089/ten.tea.2012.0762.
[45] S. Bose, D. Ke, H. Sahasrabudhe, A. Bandyopadhyay, Additive manufacturing of biomaterials, Prog. Mater. Sci. 93 (2018) 45–111, https://doi.org/10.1016/j.pmatsci.2017.08.003.
[46] S. Lu, M.A.P. McGough, B.R. Rogers, J.C. Wenke, D. Shimko, S.A. Guelcher, Resorbable nanocomposites with bone-like strength and enhanced cellular activity, J. Mater. Chem. B 5 (2017) 4198–4206, https://doi.org/10.1039/C7TB00657H.
[47] E.F. Morgan, G.U. Unnikrisnan, A.I. Hussein, Bone mechanical properties in healthy and diseased states, Annu. Rev. Biomed. Eng. 20 (2018) 119–143, https://doi.org/10.1146/annurev-bioeng-062117-121139.
[48] H.H. Bayraktar, E.F. Morgan, G.L. Niebur, G.E. Morris, E.K. Wong, T.M. Keaveny, Comparison of the elastic and yield properties of human femoral trabecular and cortical bone tissue, J. Biomech. 37 (2004) 27–35, https://doi.org/10.1016/S0021-9290(03)00257-4.
[49] D.B. Burr, C. Milgrom, D. Fyhrie, M. Forwood, M. Nyska, A. Finestone, S. Hoshaw, E. Saiag, A. Simkin, In vivo measurement of human tibial strains during vigorous activity, Bone. 18 (1996) 405–410, https://doi.org/10.1016/8756-3282(96)00028-2.
[50] W.B. Edwards, R.H. Miller, T.R. Derrick, Femoral strain during walking predicted with muscle forces from static and dynamic optimization, J. Biomech. 49 (2016) 1206–1213, https://doi.org/10.1016/j.jbiomech.2016.03.007.
[51] J.M. Struemph, A.C.M. Chong, P.H. Wooley, Evaluation of different experience levels of orthopaedic residents effect on polymethylmethacrylate (PMMA) bone cement mechanical properties, Iowa Orthop. J. 35 (2015) 193–198. https://pubmed.ncbi.nlm.nih.gov/26361465.
[52] C. Lee, in: S. Breusch, H. Malchau (Eds.), The Mechanical Properties of PMMA Bone Cement BT - The Well-Cemented Total Hip Arthroplasty: Theory and Practice, Springer Berlin Heidelberg, Berlin, Heidelberg, 2005, pp. 60–66, https://doi.org/10.1007/3-540-28924-0_6.
[53] E.J. Harper, W. Bonfield, Tensile characteristics of ten commercial acrylic bone cements, J. Biomed. Mater. Res. 53 (2000) 605–616, https://doi.org/10.1002/1097-4636(200009)53:5<605::AID-JBM22>3.0.CO;2-5.
[54] J. Yan, K.B. Clifton, J.J. Mecholsky, R.L. Reep, Fracture toughness of manatee rib and bovine femur using a chevron-notched beam test, J. Biomech. 39 (2006) 1066–1074, https://doi.org/10.1016/j.jbiomech.2005.02.016.
[55] G. Lewis, J. Nyman, H.H. Trieu, The apparent fracture toughness of acrylic bone cement: effect of three variables, Biomaterials. 19 (1998) 961–967, https://doi.org/10.1016/S0142-9612(97)00193-2.
[56] C.T. Wang, R.M. Pilliar, Fracture toughness of acrylic bone cements, J. Mater. Sci. 24 (1989) 3725–3738, https://doi.org/10.1007/BF02385763.
[57] S. Lu, M.A.P. McGough, S.M. Shiels, K.J. Zienkiewicz, A.R. Merkel, J. P. Vanderburgh, J.S. Nyman, J.A. Sterling, D.J. Tennent, J.C. Wenke, S. A. Guelcher, Settable polymer/ceramic composite bone grafts stabilize weight-bearing tibial plateau slot defects and integrate with host bone in an ovine model, Biomaterials. 179 (2018) 29–45, https://doi.org/10.1016/j.biomaterials.2018.06.032.
[58] S. Yamada, D. Heymann, J.-M. Bouler, G. Daculsi, Osteoclastic resorption of calcium phosphate ceramics with different hydroxyapatite/β-tricalcium phosphate ratios, Biomaterials. 18 (1997) 1037–1041, https://doi.org/10.1016/S0142-9612(97)00036-7.
[59] H. Burchardt, The biology of bone graft repair, Clin. Orthop. Relat. Res. 174 (1983). https://journals.lww.com/clinorthop/Fulltext/1983/04000/The_Biology_of_Bone_Graft_Repair.5.aspx.
[60] M. Bohner, L. Galea, N. Doebelin, Calcium phosphate bone graft substitutes: failures and hopes, J. Eur. Ceram. Soc. 32 (2012) 2663–2671, https://doi.org/10.1016/j.jeurceramsoc.2012.02.028.
[61] E. Marin, M.I. Briceño, C. Caballero-George, Critical evaluation of biodegradable polymers used in nanodrugs, Int. J. Nanomedicine 8 (2013) 3071–3090, https://doi.org/10.2147/IJN.S47186.
[62] S. Lyu, D. Untereker, Degradability of polymers for implantable biomedical devices, Int. J. Mol. Sci. 10 (2009), https://doi.org/10.3390/ijms10094033.
[63] A. Banerjee, K. Chatterjee, G. Madras, Enzymatic degradation of polymers: a brief review, Mater. Sci. Technol. 30 (2014) 567–573, https://doi.org/10.1179/1743284713Y.0000000503.
[64] K. Cai, Y. Delaviz, M. Banh, Y. Guo, J.P. Santerre, Biodegradation of composite resin with ester linkages: identifying human salivary enzyme activity with a potential role in the esterolytic process, Dent. Mater. 30 (2014) 848–860, https://doi.org/10.1016/j.dental.2014.05.031.
[65] B.A. Lin, F. Jaffer, M.D. Duff, Y.W. Tang, J.P. Santerre, Identifying enzyme activities within human saliva which are relevant to dental resin composite biodegradation, Biomaterials. 26 (2005) 4259–4264, https://doi.org/10.1016/j.biomaterials.2004.11.001.
[66] H.-M. Kim, H.-R. Kim, B.S. Kim, Soybean oil-based photo-crosslinked polymer networks, J. Polym. Environ. 18 (2010) 291–297, https://doi.org/10.1007/s10924-010-0174-3.
[67] Z. Ma, Y. Hong, D.M. Nelson, J.E. Pichamuthu, C.E. Leeson, W.R. Wagner, Biodegradable polyurethane ureas with variable polyester or polycarbonate soft segments: effects of crystallinity, molecular weight, and composition on mechanical properties, Biomacromolecules 12 (2011) 3265–3274, https://doi.org/10.1021/bm2007218.
[68] L. Cai, A.S. Guinn, S. Wang, Exposed hydroxyapatite particles on the surface of photo-crosslinked nanocomposites for promoting MC3T3 cell proliferation and differentiation, Acta Biomater. 7 (2011) 2185–2199, https://doi.org/10.1016/j.actbio.2011.01.034.